crystals

MDPI

Article

Adsorption Mechanism for Arsenic (V) from Aqueous Solutions by NiCoMn-LDHs@ZBC Composite Materials

Xiaochuan Geng [1], Han Yu [1], Xueqiong Zhang [2,3,*] and Heping Shi [2,3,*]

[1] College of Science, Inner Mongolia Agricultural University, Hohhot 010018, China; xiaochuandww@emails.imau.edu.cn (X.G.); yh2023@emails.imau.edu.cn (H.Y.)
[2] College of Resources and Environment, Inner Mongolia Agricultural University, Hohhot 010018, China
[3] Inner Mongolia Key Laboratory of Soil Quality and Nutrient Resource, Hohhot 010018, China
* Correspondence: lxyzxq@imau.edu.cn (X.Z.); hpshi@imau.edu.cn (H.S.)

Abstract

In this study, zinc-modified biochar (ZBC) was prepared from rose willow, and NiCoMn-LDHs@ZBC composites were synthesized using a hydrothermal method. The composites were characterized by X-ray diffraction (XRD), Brunauer–Emmett–Teller (BET) surface area analysis, scanning electron microscopy with energy-dispersive X-ray spectroscopy (SEM-EDS), transmission electron microscopy (TEM), Fourier transform infrared spectroscopy (FTIR), and X-ray photoelectron spectroscopy (XPS). The adsorption mechanism of As(V) from aqueous solution onto NiCoMn-LDHs@ZBC was investigated through a series of arsenic adsorption experiments. The effects of various experimental parameters (including adsorbent composition and ratio, adsorbent dosage, solution pH, contact time, temperature, and coexisting ions) on the adsorption capacity were evaluated. Additionally, adsorption model fitting and kinetic analysis were conducted. The results indicate that the adsorption process follows the pseudo-second-order kinetic model (linear correlation coefficient R^2 = 0.99), while the isothermal adsorption process adheres to the Langmuir model, with a maximum adsorption capacity of 159.780 mg/g. The adsorption process is primarily dominated by chemisorption and involves three pathways: first, electrostatic attraction between the material surface and arsenic-containing ions; second, ion exchange between arsenic-containing ions and interlayer carbonate ions; and third, coordination reactions between the surface hydroxyl groups (-OH) of NiCoMn-LDHs@ZBC and As, forming As-O-M inner-sphere complexes as adsorption proceeds. Furthermore, the NiCoMn-LDHs@ZBC composite exhibits relatively stable reusability, demonstrating significant potential for the treatment of arsenic pollution in water bodies.

Keywords: arsenic; adsorption; mechanism; composite materials

Check for updates

Academic Editors: Atul A. Pawar and John Parthenios

Received: 8 April 2026
Revised: 16 May 2026
Accepted: 18 May 2026
Published: 21 May 2026

Copyright: © 2026 by the authors. Licensee MDPI, Basel, Switzerland. This article is an open access article distributed under the terms and conditions of the Creative Commons Attribution (CC BY) license.

1. Introduction

In recent years, the environment has been increasingly contaminated by substantial amounts of arsenic released from human activities like mining operations, metal smelting processes, and the manufacturing of agricultural chemicals. This contamination has given rise to a pressing environmental problem that has garnered global concern [1]. As an example of a highly toxic heavy metal, arsenic typically occurs in aqueous environments in two primary forms: inorganic arsenate (As(V)) and arsenite (As(III)). The interconversion between these two arsenic species is often regulated by environmental factors present in water, including pH levels and redox potentials (Eh). Among these two forms, arsenite

(As(III)) is recognized to be more toxic and harder to eliminate compared to arsenate (As(V)). In oxygen-rich and oxidized environments, arsenate (As(V)) is the primary species present, mainly occurring as $H_2AsO_4^-$ and $HAsO_4^{2-}$ [2]. Arsenic, recognized as a type of carcinogenic substance, when continuously encountered at elevated concentrations in the environment, notably raises the risk of cancer in humans [3]. Therefore, the World Health Organization (WHO) has clearly established a maximum allowable level (MCL) of arsenic in drinking water, which is set at 10 μg/L [4].

Biochar has drawn widespread interest in the treatment of heavy metals in wastewater, thanks to its high specific surface area, well-developed pore structure, and surface featuring functional groups like carboxyl, carbonyl, and hydroxyl groups [5,6]. Nevertheless, the arsenic adsorption and elimination effectiveness of unprocessed biochar is usually not up to expectations. To address this limitation, researchers often modify biochar to adjust its structure and surface functional groups, thereby improving its ability to adsorb arsenic [7]. Chemical modification, in particular, has been widely utilized in such contexts, as it typically requires shorter processing durations, operates at lower activation temperatures, and can yield highly effective porous activated carbon [8–10]. This technique is commonly employed across various fields including adsorption, separation, and catalytic applications.

Layered double hydroxides (LDHs) are highly regarded adsorbents for arsenic removal, characterized by their distinctive cationic layered architecture, substantial specific surface area, robust adsorption potential, and remarkable ion exchange capabilities [11]. Structurally, LDHs are generally octahedral hydromagnesiumite-like layered compounds with the general formula $[M^{2+}_{1-x}M^{3+}_x(OH)_2]^{x+}(An^-)_x/n{\cdot}mH_2O$, where M^{2+} and M^{3+} stand for divalent and trivalent metal cations, including Zn^{2+}, Ni^{2+}, Mg^{2+}, Fe^{2+}, Co^{2+}, Al^{3+}, Cr^{3+}, Fe^{3+}, Mn^{3+}, etc. [12]. Here, An^- refers to interlayer anions such as Cl^-, NO_3^-, ClO_4^-, CO_3^{2-}, and x represents the molar ratio of trivalent to total metal cations, usually in the range of 0.17–0.5 [13]. However, traditional MgAl-LDHs have limitations in arsenic removal efficiency, showing relatively low capacity for arsenic ions. To address this limitation, researchers have developed modified LDHs by incorporating additional metal elements. Li et al. [14] successfully synthesized novel MgAlMn-LDHs by introducing the transition metal Mn into the layered structure of MgAl-LDHs, with a maximum adsorption capacity of 166.94 mg/g. The introduction of Mn atoms into the LDHs framework generates additional reactive sites, thereby improving the interaction efficiency between arsenic ions and the material's surface. Consequently, the ability of LDHs to remove arsenic is markedly improved.

Studies have shown that zinc-modified biochar alone has limited arsenic adsorption capacity; the maximum arsenic adsorption capacities of zinc-modified walnut shell biochar and $ZnCl_2$-activated digested sludge biochar were only 50.00 mg/g and 27.67 mg/g, respectively [15,16]. Conventional, unmodified biochar exhibits poorer arsenic removal performance; the adsorption capacities of MgAl-LDH and NiFe-LDH combined with unmodified biochar are only 26.22 mg/g and 4.38 mg/g, respectively [17,18]. Although some pure-phase hydrotalcite materials exhibit good adsorption performance—with Mg-Fe LDH and FeMnNi-LDH capable of adsorbing up to 202.43 mg/g and 240.86 mg/g of arsenic, respectively—they still suffer from drawbacks such as high production costs, a tendency to agglomerate, and poor cycle stability. Studies have shown that when LDHs are integrated with modified biochar to create composite adsorbents for arsenic removal, these materials outperform individual components, featuring notably improved arsenic adsorption capabilities and better material recyclability. Specific studies have confirmed this potential, such as a study [19] that showed Mg/Fe-LDH-activated carbon, a type of composite material, achieved an arsenic removal efficiency of 54.2%, which is notably higher than the 4.2% efficiency of unmodified activated carbon. Furthermore, even af-

ter five repeated cycles of adsorption and desorption, the arsenic adsorption capacity of Mg/Fe-LDH-activated carbon only decreased by 20%, highlighting its strong reusability in treating arsenic-contaminated aqueous solutions. Table 1 presents the literature regarding the application of materials similar to those examined in this study for arsenic adsorption. It primarily compares parameters such as the equilibrium adsorption capacity for arsenic, the best-fit adsorption model, the optimal applicable pH, and the number of cycles. Overall, the composite material synthesized in this study demonstrates the highest arsenic adsorption performance.

Table 1. Comparison of various adsorption parameters of different adsorbents.

Adsorbent	Q_{max} ($mg \cdot g^{-1}$)	Isotherm	pH	Reusability	Reference
Mg/Fe-LDH-BC	3.6	Langmuir	6.00	5	[19]
nZVZn-PCBC	37.2	Langmuir	7.00	3	[20]
Mg/Al-BC	22.7	Freundlich	7.00	-	[21]
Corn stalk BC/MgAl	10.4	Langmuir	7.00		
Corn stalk BC/ZnAl	16.1	Langmuir	7.00		[22]
Corn stalk BC/CuAl	14.9	Langmuir	7.00		
Rice husk BC/MnFe-LDH	67.1	Langmuir	7.00		
Rice husk BC/FeMn-LDO	35.6	Langmuir	3.00	-	[23]
Corn stalk BC/ZnAl-LDH	16.1	Langmuir	7.00		
Corn stalk BC/MgAl-LDH	10.4	Langmuir	7.00		
LDH-Fe Composite	90.6	Langmuir	5.00	5	[24]
FeMnMg-LDH/BC	17.3	Langmuir	<3.70	-	[25]

In this work, a new type of composite material named NiCoMn-LDHs@ZBC was successfully fabricated by employing salix mongolica, an agricultural and forestry byproduct, as the starting substance through a hydrothermal reaction process. The composite material developed in this research is composed of nickel–cobalt–manganese layered double hydroxides (with a molar ratio of 1:2:1) and zinc-modified biomass charcoal. This study focuses on evaluating its capacity to adsorb As(V) from aqueous environments, delving into the mechanisms underlying adsorption–complexation processes and identifying key factors that affect arsenic removal efficiency. By doing so, it aims to offer theoretical foundations for the development of more effective materials designed to eliminate arsenic from water sources.

2. Materials and Methods

2.1. Materials and Reagents

The chemical reagents utilized in the experiments included cobalt nitrate ($Co(NO_3)_2 \cdot 6H_2O$, A.R), nickel nitrate ($Ni(NO_3)_2 \cdot 6H_2O$, A.R), manganese nitrate ($Mn(NO_3)_2 \cdot 4H_2O$, A.R), sodium hydroxide (NaOH, A.R), sodium carbonate (Na_2CO_3, A.R), zinc chloride ($ZnCl_2$, A.R), Hydrochloric acid (HCl, A.R), all of which conformed to analytical grade standards. For the preparation of reaction solutions for As(V), ultrapure water served as the solvent. All the above reagents are from Sinopharm Group Co Ltd. (Shanghai, China). The plant material, rose willow (*Tamarix ramosissima*), was sourced from Bayannur City in Inner Mongolia. It underwent initial chopping, followed by washing with deionized water, drying in an oven at 80 °C for twelve hours, and finally grinding to a particle size of 100 mesh for subsequent use.

2.2. Preparation of NiCoMn-LDHs@ZBC Composite Materials

To prepare ZBC, firstly, three grams of rose willow powder was weighed and transferred into a 100 mL PTFE hydrothermal reactor. Subsequently, 60 mL of deionized water was added and the mixture was dissolved through ultrasonic treatment. The resulting mixture was then heated and maintained at 180 °C within an oven for a duration of 24 h to undergo the reaction. Subsequently, the resulting product was cooled down, washed, and then dried at 80 °C to yield hydrothermally synthesized rose willow biochar (BC). Subsequently, the rose willow BC was combined with $ZnCl_2$ in a 1:1 mass ratio. The mixture was ultrasonically dispersed in deionized water, stirred at 25 °C for 6 h, and subsequently dried at 100 °C. After undergoing grinding and sieving, the mixture was transferred into a tube furnace. Subsequently, the mixture was heated from room temperature to 500 °C at a heating rate of 10 °C per minute and maintained under a nitrogen atmosphere for a duration of 60 min for pyrolysis. Following this thermal treatment, the material was cooled down to ambient temperature, subsequently immersed in 3 M hydrochloric acid for activation purposes, and then repeatedly rinsed with deionized water until the resulting washings reached a neutral pH level. Subsequently, the treated substance was dried, ground into fine particles, and passed through a sieve to prepare zinc-modified biochar (ZBC).

To prepare the NiCoMn-LDHs@ZBC composite material (Figure 1), first weigh the required amounts of $(Ni(NO_3)_2{\cdot}6H_2O)$, $(Co(NO_3)_2{\cdot}6H_2O)$ and $(Mn(NO_3)_2{\cdot}4H_2O)$, according to their respective masses, ensuring a molar ratio of 1:2:1. Then, place the weighed salts into a 50 mL beaker for mixing. Subsequently, dissolve the nitrates and add ZBC at a mass ratio of 1:5 (LDHs to BC). The mixture is then subjected to ultrasonication to form Solution A. Meanwhile, weigh 0.68 g of sodium hydroxide (NaOH) and 1.06 g of sodium carbonate (Na_2CO_3) in another 50 mL beaker, and dissolve them to prepare Solution B. Next, place Solution A in an 80 °C constant-temperature water bath and allow the reaction to proceed under vigorous stirring. Slowly add Solution B dropwise into Solution A until the pH reaches 9.0. Stir the resulting mixture for 30 min, then transfer it to a PTFE hydrothermal reactor. React at 120 °C for 24 h. After hydrothermal treatment, allow the mixture to cool to room temperature, followed by vacuum filtration to separate the precipitate. Wash the precipitate repeatedly with ultrapure water until the filtrate reaches a neutral pH. Subsequently, transfer the obtained solid to a vacuum drying oven and dry at 80 °C for 12 h to ultimately obtain the NiCoMn-LDHs@ZBC composite material as the final product.

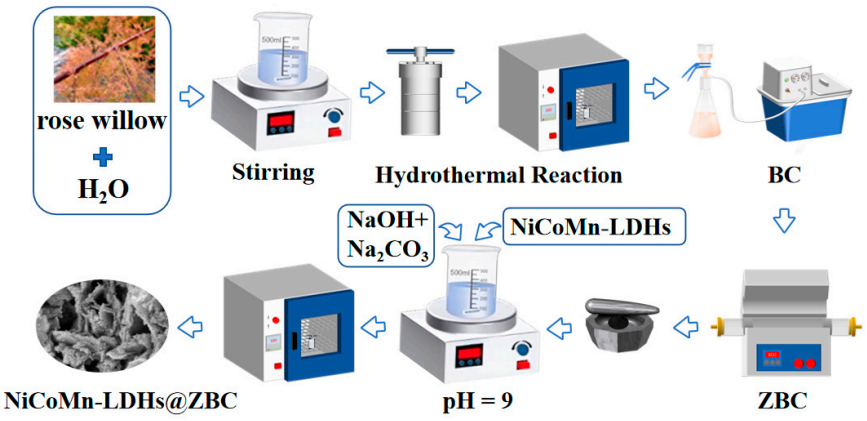


Figure 1. The specific synthesis steps of NiCoMn-LDHs@ZBC.

2.3. Characterization

X-ray diffraction (XRD) measurements were conducted using CuKα radiation on a Philips APD 3720 instrument (Philips Electronic Instruments, Mahwah, NJ, USA) to identify the minerals present on the biochar surface and to determine the crystal structure of the

layered double hydroxides (LDHs). Additionally, the specific surface area of the samples was analyzed using NOVA 1200 analyzer (Quantachrome Instruments, Boynton Beach, FL, USA). These characterizations were performed under stringent experimental conditions: samples were degassed at 300 °C for 300 min, using a pre-treatment mass exceeding 100 mg, followed by adsorption at 77.3 K (liquid nitrogen temperature). Furthermore, the surface morphology of the composites was examined using scanning electron microscopy (SEM) (JEOL JSM-6400, Tokyo, Japan). To complement these observations, the elemental composition and spatial distribution of cobalt (Co), manganese (Mn), and nickel (Ni) on the biochar surface were analyzed using energy-dispersive X-ray spectroscopy (EDS) (Oxford Instruments, Xplore 30, High Wycombe, UK). The elemental composition and valence states on the biochar surface were further investigated in detail using X-ray photoelectron spectroscopy (XPS) (PHI 5100 series ESCA spectrometer, Perkin-Elmer, Shelton, CT, USA). Moreover, detailed information regarding the morphology and size of the materials was obtained through transmission electron microscopy (TEM). Fourier transform infrared spectroscopy (PerkinElmer Spectrum, ICE3000, Waltham, MA, USA) was employed to identify the functional groups present in the material. Finally, an atomic fluorescence spectrometer (Puxi General Instrument Co., Ltd., PF6-2, Beijing, China) was utilized to assess the arsenic content.

2.4. Adsorption Experiment

Batch adsorption studies were performed to explore the adsorption capacity, contributing elements, and underlying mechanisms of As(V) removal by BC, ZBC, and NiCoMn-LDHs@ZBC materials [26]. These experiments were carried out in 50 mL sealed conical flasks under ambient temperature conditions (25 ± 2 °C), with the concentration of As(V) measured via atomic fluorescence spectrophotometry. To explore the adsorption performance of these materials, a series of influencing factors were studied, including adsorbent dosage, solution pH, temperature, and the presence of coexisting ions. Furthermore, the investigation of adsorption kinetics is crucial for the design of efficient adsorption systems. It is essential to correlate the experimental data with established mathematical models, during which specific parameter values must be determined, such as the adsorption capacity of the material at equilibrium. Each of these samples underwent testing with a triplicate measurement method to ensure data reliability. The amount of arsenic adsorbed by the adsorbent from aqueous solutions was determined by applying Equation (1) [27]:

$$q_e = \frac{(c_0 - c_e)V}{m} \quad (1)$$

In the equation, q_e (mg/g) represents the adsorption capacity of the material, c_0 and c_e denote the initial concentration and equilibrium concentration of As(V) in the solution (mg/L), respectively, V is the volume of the solution (L), and m is the dosage of the adsorbent material (g).

3. Results and Discussion

3.1. Characterization of NiCoMn-LDHs@ZBC

According to the X-ray diffraction analysis results presented in Figure 2a, the diffraction peak observed at 25.2° for Zn-modified rose willow (ZBC) is attributed to the (002) crystal plane reflection of amorphous carbon, which represents a characteristic peak of a disordered graphite structure. The position in the ZBC spectrum is marked with plum blossom symbol (♣). This finding indicates that Zn modification did not alter the structure of the biochar. The characteristic peaks of NiCoMn-LDH at 11.58°, 22.93°, and 34.23° correspond to the (003), (006), and (012) crystal planes of the hydrotalcite-like layered structure,

respectively, and are consistent with the PDF#51-1525 card data. After loading NiCoMn-LDH onto ZBC, the XRD pattern of the resulting NiCoMn-LDH@ZBC demonstrates that the loading process did not affect the structure of NiCoMn-LDH. The relatively weak characteristic peaks of ZBC in NiCoMn-LDH@ZBC may be attributed to the low content of ZBC in the composite. In addition, The ternary layered double hydroxide (NiCoMn-LDH) with a molar ratio of Ni:Co:Mn = 1:2:1 is typically characterized by carbonate (CO_3^{2-}) intercalation in its interlayer structure. A literature report [28] indicates that the theoretical interlayer spacing for this NiCoMn-LDH composition is calculated to be between 0.75 and 0.78 nm. The interlayer spacing of the sample was determined based on the XRD analysis of NiCoMn-LDHs@ZBC. By selecting the (003) crystal plane diffraction peak ($2\theta = 11.58°$) and applying the Bragg equation ($2d \sin\theta = \lambda$, where $\lambda = 0.154$ nm), the actual interlayer spacing of the sample was found to be 0.764 nm. This calculated value falls precisely within the theoretical interlayer spacing range (0.75–0.78 nm) for the Ni:Co:Mn = 1:2:1 ternary LDH with carbonate intercalation, indicating that the prepared sample successfully formed a typical layered double hydroxide structure, with carbonate anions as the main interlayer species, which aligns closely with the theoretical structural characteristics.

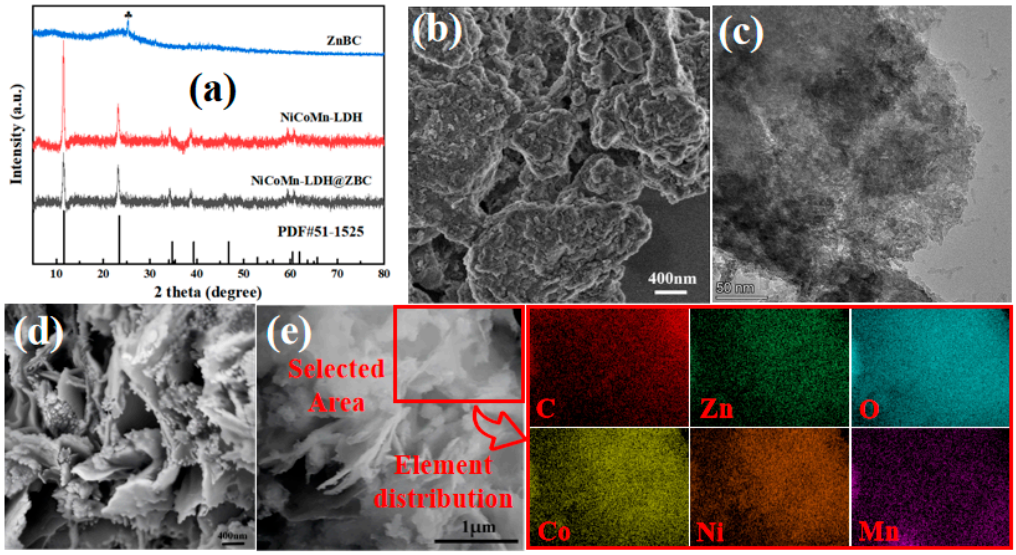


Figure 2. (**a**) XRD patterns of ZnBC, NiCoMn-LDHs and NiCoMn-LDHs@ZBC; (**b**) SEM image of the NiCoMn-LDHs; (**c**) TEM image of the NiCoMn-LDHs; (**d**) SEM image of the NiCoMn-LDHs@ZBC; (**e**) The red box indicates the SEM region of NiCoMn-LDHs@ZBC, while the right side displays the corresponding elemental distribution maps for the selected area.

Figures 2b and 2c display the scanning electron microscopy (SEM) image and transmission electron microscopy (TEM) image of NiCoMn-LDH, respectively. The results indicate that NiCoMn-LDHs exhibits a sheet-like morphology, although pronounced stacking phenomena are observed. The fragmented structure of NiCoMn-LDHs can be seen at the edges in Figure 2c. Overall, the agglomeration phenomenon remains remarkably evident. The SEM image of NiCoMn-LDHs@ZBC, obtained by loading NiCoMn-LDHs onto ZnBC (Figure 2d), demonstrates that the addition of ZnBC significantly alleviates the agglomeration phenomenon of NiCoMn-LDH, presenting a structure in which NiCoMn-LDHs is embedded within ZnBC (Figure S1). To further investigate the distribution of each element, selected area analysis via SEM-Mapping was performed on NiCoMn-LDHs@ZBC. As shown in Figure 2e, the elemental distribution in the selected area of the material is highly uniform, indicating that NiCoMn-LDHs@ZBC has been successfully composited.

Figure 3a presents the adsorption–desorption isotherm of the NiCoMn-LDHs@ZBC composite material, which exhibits Type IV characteristics typical of mesoporous materi-

als. The blue curve represents the nitrogen adsorption curve, illustrating the process by which the number of nitrogen molecules adsorbed on the material surface (the adsorption amount) gradually increases as the relative pressure of nitrogen (P/P_0) rises from 0 to 1.0. Conversely, the yellow curve depicts the nitrogen desorption curve, which indicates the process in which nitrogen molecules on the material surface and within the pores gradually desorb, leading to a decrease in the adsorption amount as the relative pressure of nitrogen (P/P_0) decreases from 1.0. In the range of $P/P_0 < 0.3$, the adsorption capacity increases rapidly with rising relative pressure, a phenomenon attributed to monolayer and multilayer nitrogen adsorption on the material surface. This observation indicates the presence of abundant micropores or small mesopores in the sample, which provide numerous active adsorption sites. The curve displays a H_2-type hysteresis loop ($P/P_0 > 0.4$), indicating the presence of both mesopores and slit-like pores in the adsorbent [29]. According to the pore size distribution analysis in Figure 3b, the average pore size is approximately 2.97 nm. This structural characteristic not only endows the material with a well-developed porous framework and a higher specific surface area but also facilitates effective arsenic capture and removal [30].

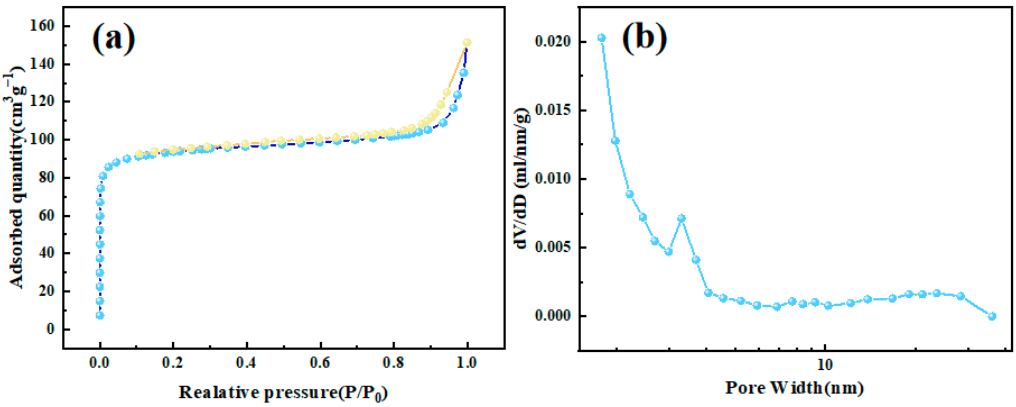


Figure 3. (**a**) Nitrogen adsorption-desorption isotherm of the NiCoMn-LDHs@ZBC; (**b**) Pore size distribution curve of the NiCoMn-LDHs@ZBC.

Table 2 presents a comparison of specific surface area data for various materials. The specific surface area (S_{BET}) of ZBC is 226.4 m^2/g (Figure S2a), while that of NiCoMn-LDHs is 126.7 m^2/g (Figure S3a). Following their combination, the composite material NiCoMn-LDHs@ZBC exhibits an increased S_{BET} of 284.2 m^2/g. This enhancement in specific surface area can significantly improve the adsorption capacity of material. In terms of average pore size, ZBC has an average pore size of approximately 3.88 nm (Figure S2b), whereas NiCoMn-LDHs exhibit a larger average pore size of about 8.53 nm (Figure S3b) due to their fragmented structure. The composite material NiCoMn-LDHs@ZBC demonstrates a reduced average pore size centered around 2.97 nm, which can be attributed to the embedded structure of the fragmented NiCoMn-LDHs and ZBC. The BET results align with the structural characterization of the materials.

Table 2. Specific surface area and pore size of materials.

Sample	S_{BET} (m^2/g)	V_{pore} (cm^3/g)	R_{Avg} (nm)
ZBC	226.4	0.22	3.88
NiCoMn-LDHs	126.7	0.27	8.53
NiCoMn-LDHs@ZBC	284.2	0.21	2.97
NiCoMn-LDHs@ZBC-As(V)	198.7	0.23	4.64

3.2. Adsorption Test

Figure 4a presents the arsenic adsorption performance of various materials under identical conditions. The equilibrium adsorption capacity data indicates that pure-phase biochar (BC) and layered double hydroxides (LDHs) exhibit relatively poor arsenic adsorption performance. In contrast, zinc-modified biochar (ZBC) demonstrates enhanced arsenic adsorption capability compared to BC. Furthermore, the composite material NiCoMn-LDHs@ZBC, formed by combining NiCoMn-LDHs with ZBC, shows a significantly improved arsenic adsorption capacity compared to pure-phase materials. To optimize the composition of the composite material, synthesis conditions, and adsorption time, we conducted a series of experiments. Initially, we investigated the ratio of the three metal elements in NiCoMn-LDHs. The results indicated that the adsorption performance was optimal when the molar ratio of Ni, Co, and Mn was 1:2:1 (Figure S4a). Additionally, we examined the synthesis temperature of NiCoMn-LDHs, with data revealing that the material exhibited the best adsorption performance when synthesized at 120 °C (Figure S4b). Finally, we studied the effect of adsorption time on adsorption capacity, with results demonstrating that the adsorption performance peaked after 24 h (Figure S4c).

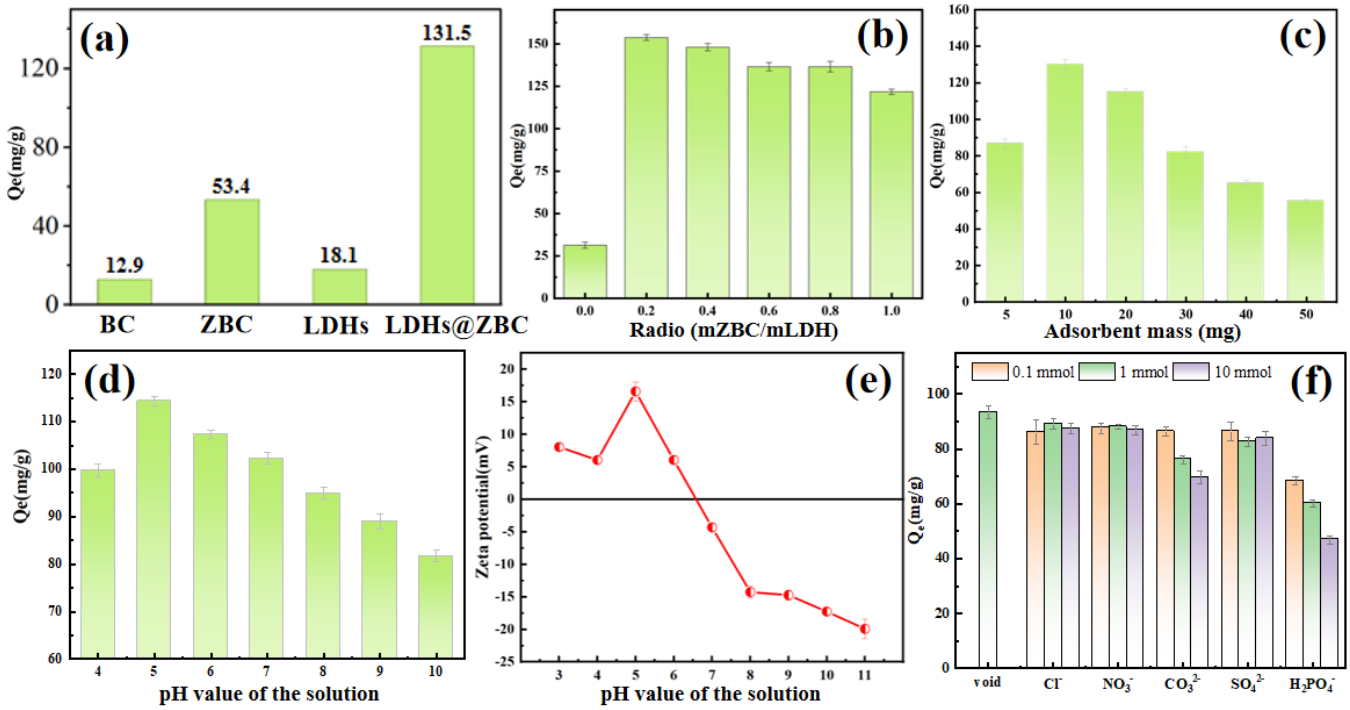


Figure 4. Adsorption Experiments: (**a**) Equilibrium adsorption capacity data of different materials for As under identical conditions (pH = 7, c_0 = 100 mg/L, m=10 mg, temperature = 25 °C, and time = 24 h). (**b**) Effect of the mass ratio of ZBC and LDHs in NiCoMn-LDHs@ZBC on arsenic adsorption (pH = 5, c_0 = 100 mg/L, temperature = 25 °C, and time = 24 h). (**c**) Effect of adsorbent mass on arsenic adsorption (pH = 5, c_0 = 100 mg/L, temperature = 25 °C, and time = 24 h). (**d**) Effect of pH on arsenic adsorption (adsorbent dosage = 10 mg, temperature = 25 °C, time = 24 h, and solution concentration = 300 mg/L). (**e**) The variation in zeta potential (ξ) of NiCoMn-LDHs@ZBC with aqueous solution pH (pH 3–11). (**f**) Effect of different anions on arsenic adsorption (pH = 5, dosage = 10 mg, c_0 = 100 mg/L, temperature = 25 °C, and time = 24 h).

Figure 4b illustrates the effect of the mass ratio between ZBC and NiCoMn-LDHs in the NiCoMn-LDHs@ZBC composite on the material's adsorption capacity. The results indicate that optimal adsorption performance is achieved when the mass ratio of ZBC to NiCoMn-LDHs is 0.2. Figure 4c depicts the variation in As(V) adsorption capacity with the dosage of the NiCoMn-LDHs@ZBC composite. At a dosage of 10 mg, the composite material

demonstrates the highest adsorption capacity for As(V). The pH of the solution plays a crucial role in determining the speciation of arsenic and the surface charge characteristics of the adsorbent, which are primarily influenced by the functional groups present on the adsorbent surface [31]. Therefore, investigating the effect of solution pH on arsenic adsorption capacity is crucial. The results indicate that optimal adsorption occurs at pH = 5. At this specific pH level, arsenate (As(V)) predominantly existed in the forms of $H_2AsO_4^-$ and $HAsO_2^-$, which enhanced its interaction with the composite's surface sites, thereby promoting the adsorption process. Conversely, a reduction in adsorption efficiency is observed when the solution's hydrogen ion concentration decreases, which corresponds to an elevation in pH levels. When the solution pH rises to a higher level, arsenate (V) species in the system predominantly take the forms of $H_2AsO_4^-$ and AsO_4^{3-}. With the gradual escalation of OH^- ion concentration in the environment, the anionic arsenate particles start to engage in competitive adsorption with OH^- ions at the material's surface active sites. The OH^- ions adsorbed onto the material surface can trigger electrostatic repulsion, which in turn lowers the material's ability to adsorb arsenate anions [31–33]. To elucidate the influence of pH on the adsorption process, the zeta potential values of the adsorbent in aqueous solution at different pH levels were measured. As shown in Figure 4e, the point of zero charge (PZC) of NiCoMn-LDHs@ZBC is 6.6. This indicates that when pH < 6.6, the surface of NiCoMn-LDHs@ZBC becomes positively charged due to protonation, while at pH > 6.6, the surface undergoes deprotonation and gradually becomes negatively charged. The high adsorption capacity at lower pH values (pH < PZC) is primarily attributed to potential electrostatic interactions between the material and arsenate anions. As the solution pH increases, the number of positively charged sites decreases while the number of negatively charged sites increases. Concurrently, the rising concentration of OH^- ions in the solution competes with arsenate anions, leading to a decline in adsorption performance.

Additionally, interfering anions such as Cl^-, NO_3^-, CO_3^{2-}, SO_4^{2-}, and $H_2PO_4^-$ were introduced by adding NaCl, $NaNO_3$, Na_2CO_3, Na_2SO_4, and $NaH_2PO_4{\cdot}2H_2O$. As shown in Figure 4f, the effects of these anions on arsenic adsorption were investigated at various concentrations (0 mM, 0.1 mM, 1 mM, and 10 mM). According to the experimental data, it is noteworthy that when the $H_2PO_4^-$ concentration increased from 0 to 0.1 mM, the adsorption capacity of As(V) significantly decreased from 93.69 mg/g to 68.06 mg/g, representing a reduction of 27.36%. This phenomenon can be attributed to the structural similarity between $H_2PO_4^-$ and $H_2AsO_4^-$, which results in comparable adsorption characteristics. The phosphate ions ($H_2PO_4^-$) interact with the surface -OH of NiCoMn-LDHs@ZBC to form more stable complexes, thereby occupying potential adsorption sites [34,35]. Deng et al. [36] demonstrated that as the concentration of CO_3^{2-} increases, the arsenic adsorption capacity initially decreases and then stabilizes, which occurs after carbonate ions occupy and deplete the surface adsorption sites. This is likely due to competitive adsorption between carbonate ions and arsenate for the existing active sites on the surface of NiCoMn-LDHs@ZBC. In contrast, the coexistence of SO_4^{2-}, NO_3^-, and Cl^- had negligible effects on As(V) removal, primarily because these coexisting anions bind to the material mainly through electrostatic interactions [37].

To investigate the relationship between adsorption capacity and temperature, we conducted adsorption temperature optimization experiments at five distinct temperature points: 25 °C, 30 °C, 35 °C, 40 °C, and 45 °C. As illustrated in Figure 5a, the adsorption capacity increased with rising temperature. Considering the practical applications of the adsorbent and associated energy consumption issues, we established an upper temperature limit of 45 °C. This paper primarily focuses on the performance of the adsorbent at 25 °C. The influence of temperature on adsorption capacity underscores its significant

role in this process. To explore the thermodynamic characteristics of the adsorption process, we calculated adsorption isotherms at these five temperatures. Figure 5b depicts the relationship between the thermodynamic equilibrium constant K_d and temperature T, with $1/T$ plotted on the x-axis and $\ln K_d$ on the y-axis. The fitting results indicate that $\ln K_d = -26.79(1/T) + 0.44$. According to the relationship between $\ln K_d$, enthalpy change ΔH, and entropy change ΔS ($\ln K_d = -\Delta H/RT + \Delta S/R$), the calculated values are $\Delta H = 0.22$ kJ·mol^{-1} and $\Delta S = 3.66$ J·mol^{-1}·K^{-1}.

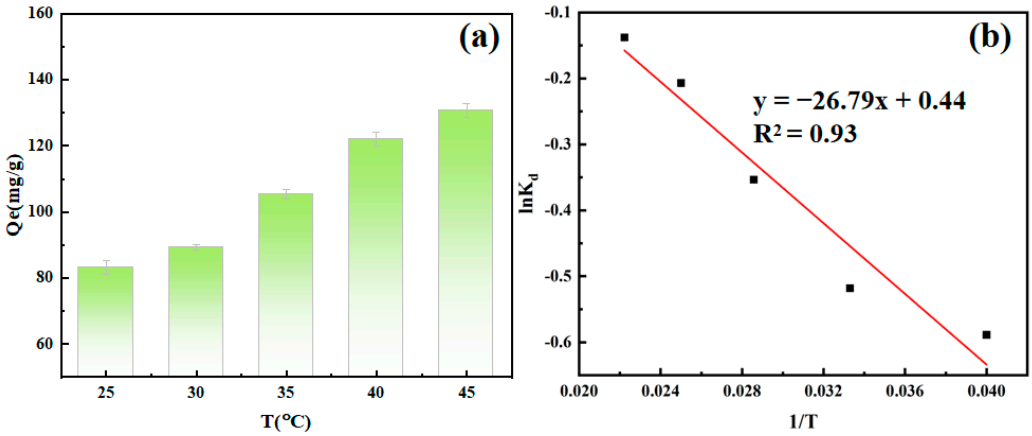


Figure 5. Adsorption Experiments: (**a**) Effect of temperature on As adsorption capacity (pH = 5, c_0 = 100 mg/L, adsorption time = 24 h). (**b**) The relationship between the thermodynamic equilibrium constant K_d and temperature T. For each temperature (T), K_d is calculated based on experimental data using the formula $K_d = q_e/c_e$, where q_e represents the adsorption amount on the adsorbent at equilibrium (mg/g), and c_e denotes the concentration of the pollutant in the solution at equilibrium (mg/L).

Furthermore, based on the Gibbs–Helmholtz equation ($\Delta G = \Delta H - T\Delta S$), we calculated the Gibbs free energy at different temperatures (Table 3). According to the adsorption thermodynamic parameters presented in Table 2, it can be concluded that the adsorption process is endothermic, increases entropy, and occurs spontaneously. According to thermodynamic data, the adsorption capacity of arsenic increases with rising temperature, indicating that elevated temperatures can promote the adsorption process. Thermodynamic studies of the adsorption process provide a foundational dataset for establishing a thermodynamic–kinetic coupling model, which facilitates the rapid screening of optimal adsorption systems. This approach enables precise control and real-time optimization of arsenic removal processes, thereby offering a theoretical basis for industrial arsenic removal.

Table 3. Thermodynamic parameters of adsorption process.

Parameters	**Relevant Data**				
T (°C)	25	30	35	40	45
ΔH (kJ·mol^{-1})			0.223		
ΔS (J·mol^{-1}·K^{-1})			3.66		
ΔG (kJ·mol^{-1})	−0.868	−0.887	−0.905	−0.923	−0.941

3.3. Adsorption Isotherm

Adsorption, recognized as an efficient, economical, and environmentally friendly technology for pollutant treatment, is widely applied to remove heavy metal ions, organic pollutants, and other contaminants from water bodies and soils. Evaluating its adsorption performance and investigating its mechanisms are essential prerequisites for the industrial application of this technology. In the realm of adsorption thermodynamics research, ad-

sorption isotherm models serve as key tools for describing the quantitative relationship between the adsorption capacity of adsorbents for pollutants and their equilibrium concentration. Among these models, the Langmuir and Freundlich isotherms have emerged as the two most widely used and classic models in the field of adsorption due to their simplicity, applicability, and interpretability. Biosorbents (such as microorganisms, plant straw, and chitosan) and abiotic sorbents (such as activated carbon, zeolite, and nanomaterials) represent two mainstream types of adsorption materials, exhibiting significant differences in pollutant adsorption mechanisms (e.g., monolayer adsorption, multilayer adsorption, physical adsorption, and chemical adsorption) due to variations in their structural characteristics (e.g., specific surface area, active sites, and pore size distribution). The Langmuir isotherm is predicated on the assumptions of a uniform adsorbent surface, the presence of single adsorption sites, a monolayer reversible adsorption process, and the absence of interactions between adsorbate molecules. This model effectively illustrates the saturated adsorption capacity and adsorption affinity of an adsorbent, rendering it particularly suitable for characterizing adsorption processes that are predominantly governed by monolayer chemical adsorption on relatively homogeneous surfaces of non-biological adsorbents, such as activated carbon and molecular sieves. The fitting parameters derived from this model can be directly utilized to assess the upper limits of adsorption performance and the adsorption strength of the adsorbent, thereby providing clear guidance for the modification of non-biological adsorbents, such as enhancing specific surface area or increasing active sites. Conversely, the Freundlich isotherm is an empirical model that does not necessitate the assumption of adsorbent surface homogeneity. This model is more adept at describing adsorption processes involving biosorbents, such as microbial cells and plant fibers, which exhibit significant surface heterogeneity, where multilayer physical adsorption or combined chemical adsorption predominates. The fitting parameters of the Freundlich isotherm can effectively reflect the nonlinearity of the adsorption process and the variation in adsorption capacity with concentration, thereby characterizing the complex adsorption behaviors of biosorbents that arise from their porous structures and functional group diversity.

Equation (2) [38] is the Langmuir adsorption isotherm equation.

$$Q_e = \frac{Q_m K_L C_e}{1 + K_L C_e} \tag{2}$$

Q_e is the adsorption capacity at equilibrium, Q_m is the theoretical adsorption capacity, K_L is the equilibrium constant for the adsorption reaction, and C_e is the concentration of the adsorbate at equilibrium.

Equation (3) [39] is the Freundlich isotherm equation.

$$lnQ_e = \frac{1}{n} lnC_e + lnK_F \tag{3}$$

K_L and K_F represent the Freundlich constants here, with the parameter n serving as the heterogeneous factor within the Freundlich isotherm model.

To analyze the adsorption behavior, the study employed both Langmuir and Freundlich isothermal adsorption models for linear and nonlinear fitting. As shown in Figure 6a, the adsorption capacity of NiCoMn-LDHs@ZBC for arsenate increases with the initial arsenate concentration. The fitting results demonstrate that the Langmuir adsorption model yields a higher correlation coefficient (R^2 = 0.996) compared to the Freundlich model (R^2 = 0.943), suggesting that the adsorption process is better described by the Langmuir model. As depicted in Figure 6b,c, the linear fitting indicates that the Langmuir model (R^2 = 0.996) exhibits a higher correlation coefficient than the Freundlich model

(R^2 = 0.933). This trend illustrates that the Langmuir model can more accurately characterize the isothermal adsorption process of As(V), suggesting that arsenic adsorption by the NiCoMn-LDHs@ZBC composite primarily occurs through monolayer adsorption on a homogeneous surface. This phenomenon may be attributed to the highly uniform distribution of active sites on the material's surface, with a theoretical adsorption capacity reaching 159.780 mg/g. When the Freundlich model was employed to fit the data, the calculated 1/n value was found to be less than 1, indicating that the material exhibits a strong affinity for arsenic adsorption and that the predominant mechanism of this process is chemical in nature.

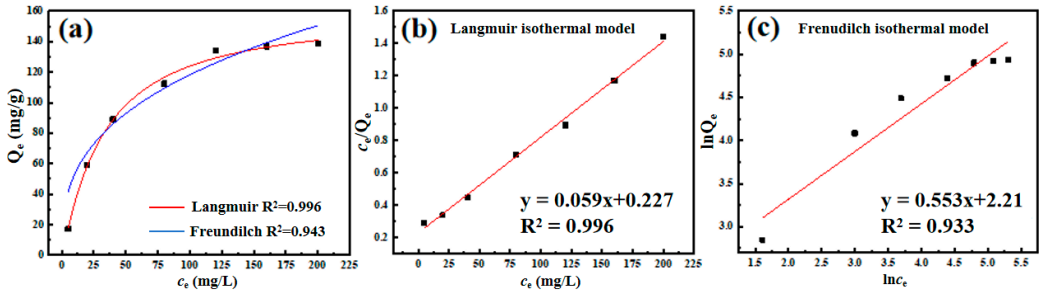


Figure 6. (**a**) Nonlinear fitting of Langmuir and Freundlich adsorption isotherms (pH = 5, dosage = 10 mg, c_0 = 100 mg/L, temperature = 25 °C, and time = 24 h). In the figure, the black dots represent the equilibrium adsorption amount (Q_e) corresponding to each initial concentration. The formula for Q_e is given by $Q_e = (c_0 - c_e) * V/m$, where c_0 denotes the initial concentration of the pollutant in the solution (mg/L), c_e is the remaining concentration of the pollutant in the solution at adsorption equilibrium (mg/L), V is the volume of the solution (L), and m is the mass of the adsorbent added (g). (**b**) Linear fitting of Langmuir adsorption isotherm. (**c**) Linear fitting of Freundlich adsorption isotherm.

3.4. Adsorption Kinetics

This paper primarily discusses the fitting of the pseudo-first-order kinetic model, pseudo-second-order kinetic model, Weber–Morris intraparticle diffusion model, and Boyd model in the context of adsorption kinetics. The fundamental assumption of pseudo-first-order kinetics is that the adsorption rate is proportional to the number of unoccupied adsorption sites, typically associated with physical adsorption that involves van der Waals forces and diffusion control. In contrast, the core assumption of pseudo-second-order kinetics posits that the adsorption rate is proportional to the square of the number of unoccupied sites, which corresponds to chemisorption involving chemical bonds, ion exchange, and strong interactions. Additionally, the comprehensive analysis results of the Weber–Morris and Boyd models are particularly utilized to determine whether the rate-limiting step of the adsorption process is intraparticle diffusion or film diffusion.

Pseudo-first-order Equation (4), which is alternatively referred to as the Lagergren equation, can be formulated as follows:

$$\ln(q_e - q_t) = lnq_e - k_1 t \tag{4}$$

Pseudo-second-order Equation (5) [40]: This type of kinetic model was initially introduced by Blanchard et al.

$$\frac{t}{q_t} = \frac{1}{(k_2 q_e^2)} + \frac{t}{q_e} \tag{5}$$

In Equations (4) and (5), q_e denotes the equilibrium adsorption capacity (mg·g^{-1}), while q_t represents the adsorption amount at time t (mg·g^{-1}). The adsorption time is denoted by t (min). k_1 and k_2 are the pseudo-first-order and pseudo-second-order kinetic constants, with units of min^{-1} and g·(mg·min)$^{-1}$, respectively.

Figure 7a illustrates the nonlinear fitting of pseudo-first-order and pseudo-second-order kinetics for the arsenic adsorption process using NiCoMn-LDHs@ZBC. Based on the fitting correlation coefficients, the adsorption process aligns more closely with the pseudo-second-order kinetic model (R^2 = 0.977) than with the pseudo-first-order kinetic model (R^2 = 0.950). Figure 7b,c display the linear fitting results for pseudo-first-order and pseudo-second-order kinetics, respectively. The fitting correlation coefficient R^2 for pseudo-first-order kinetics is 0.824, while that for pseudo-second-order kinetics is 0.998. Consequently, the arsenic adsorption process by NiCoMn-LDHs@ZBC is predominantly governed by chemical mechanisms, suggesting that NiCoMn-LDHs@ZBC captures arsenic primarily through chemical interactions rather than physical means.

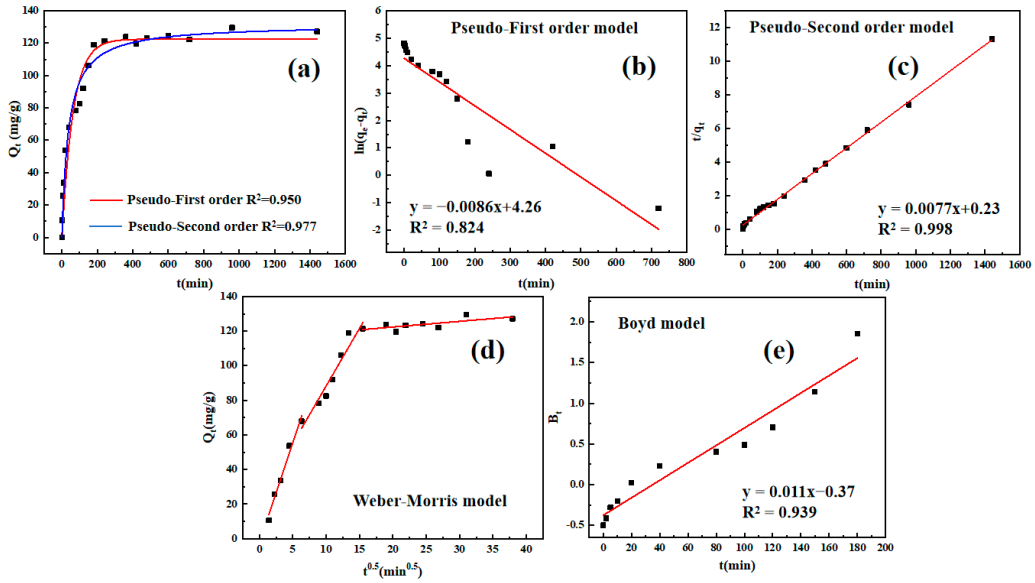


Figure 7. (**a**) Nonlinear fitting of pseudo-first-order and pseudo-second-order adsorption kinetic models (pH = 5, dosage = 10 mg, c_0 = 100 mg/L, temperature = 25 °C, and time = 24 h). In the figure, the black dots represent the instantaneous adsorption amount (Q_t) corresponding to each adsorption time point. The formula for calculating Q_t is given by $Q_t = (c_0 - c_t) * V/m$, where c_0 denotes the initial concentration of the pollutant in the solution (mg/L), c_t represents the residual concentration of the pollutant in the solution at time t (mg/L), V indicates the volume of the solution (L), and m signifies the mass of the added adsorbent (g). (**b**) Linear fitting of the pseudo-first-order adsorption kinetic model. (**c**) Linear fitting of the pseudo-second-order adsorption kinetic model. (**d**) Linear fitting of the Weber–Morris intraparticle diffusion model. (**e**) Linear fitting of the Boyd model.

Furthermore, the Weber–Morris intraparticle diffusion model was employed to analyze the adsorption process (Figure 7d). The fitting results indicate that arsenic adsorption can be categorized into three stages: surface diffusion, intraparticle diffusion, and adsorption–desorption equilibrium. In the initial stage of adsorption, arsenic ions rapidly occupy the adsorption sites on the material's surface, being adsorbed through electrostatic or complexation interactions [41]. Due to the large specific surface area and high porosity of the NiCoMn-LDHs@ZBC composite, it effectively adsorbs arsenic. In the second stage of the adsorption process, as the surface layer approaches saturation and the available adsorption sites diminish, arsenic ions in the outer layer further diffuse into the internal pores. The narrow channels increase diffusion resistance, resulting in a decrease in the adsorption rate [14]. In the third stage, only a small amount of arsenic is adsorbed and desorbed, reaching saturation [18]. The fitted straight line does not pass through the origin, indicating that the adsorption process is not solely governed by intraparticle diffusion.

The fitting data of the Weber–Morris intraparticle diffusion model and the Boyd model (Table 4) indicate that the adsorption process of NiCoMn-LDHs@ZBC for the target pol-

lutant can be divided into three distinct stages. The first stage is characterized by rapid liquid film diffusion, with k_{i1} = 11.61 and R_1^2 = 0.97. The second stage represents the rate-limiting intraparticle diffusion phase, where the rate constant decreases to k_{i2} = 6.65 and R_2^2 = 0.93. The third stage is the adsorption equilibrium stage, marked by a significant reduction in the rate. The intercept c values for all stages are non-zero, suggesting that the adsorption process is not solely governed by intraparticle diffusion. To elucidate the rate-controlling mechanism, the Boyd model [42] was further employed for analysis. The fitting results shown in Figure 7e indicate that the linear fitting intercept of B_t versus t significantly deviates from the origin, with R^2 = 0.94 (Table 4). This suggests that liquid film diffusion is the rate-limiting step controlling the entire adsorption process, while intraparticle diffusion serves as an auxiliary rate-controlling factor in the later stages. These findings are consistent with the conclusions drawn from the Weber–Morris intraparticle diffusion model fitting. Based on this analysis, it can be concluded that the entire adsorption process is simultaneously influenced by both liquid film diffusion and intraparticle diffusion, with intraparticle diffusion in the second stage being the primary rate-limiting step throughout the process. During this rate-limiting step, chemical bonds are formed between the surface hydroxyl groups of the NiCoMn-LDHs@ZBC adsorbent and the arsenic adsorbate [36]. Furthermore, literature reports indicate that these interactions may lead to the formation of inner-sphere complexes [43].

Table 4. Fitting parameters of the Weber–Morris intraparticle diffusion model and the Boyd model.

	Weber–Morris Model									**Boyd Model**		
Parameters	k_{i1}	c_1	R_1^2	k_{i2}	c_2	R_2^2	k_{i3}	c_3	R_3^2	a	b	R^2
Value	11.61	2.52	0.97	6.65	21.77	0.93	0.33	115.86	0.47	0.01	−0.37	0.94

3.5. Adsorption Mechanism

To further investigate the adsorption mechanism, a series of characterizations were performed on the materials both before and after adsorption. Firstly, SEM characterization was conducted on NiCoMn-LDHs@ZBC following As adsorption. The results shown in Figure S5 indicate that the morphology of NiCoMn-LDHs@ZBC remained unchanged post-As adsorption. Additionally, Figure 8 presents the FTIR spectra of various materials, including NiCoMn-LDHs@ZBC, both before and after As adsorption.

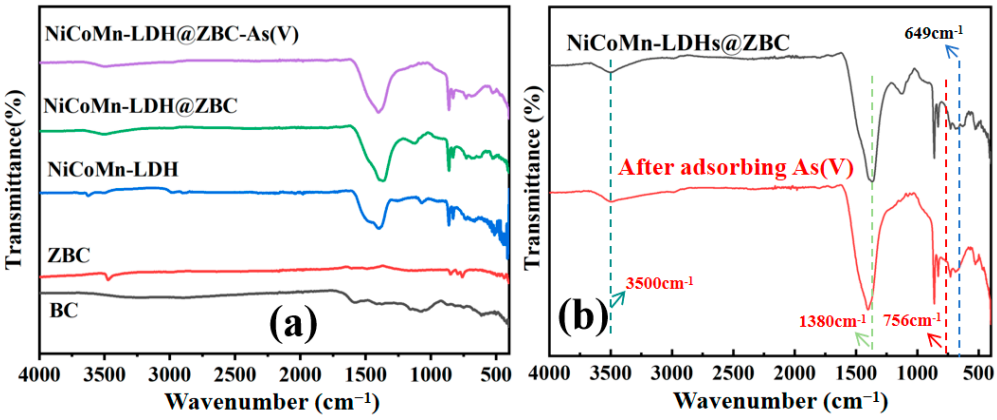


Figure 8. (**a**) Comparison of FTIR spectra for different materials; (**b**) FTIR spectra of the NiCoMn-LDHs@ZBC before and after arsenic adsorption.

The infrared spectra of BC and ZBC displayed overall gradual changes, with only weak characteristic absorptions of C-O and C=C functional groups in the 1600–1000 cm^{-1} range,

consistent with the infrared features of biochar materials. This suggests that zinc modification (ZBC) did not significantly alter the skeletal structure of the biochar. For NiCoMn-LDH, the broad peak near 3500–3200 cm^{-1} corresponds to the stretching vibrations of interlayer water and hydroxyl groups (-OH). The peak near 1630 cm^{-1} is attributed to the bending vibration of interlayer water molecules, while the peak near 1380 cm^{-1} is assigned to the asymmetric stretching vibration of interlayer carbonate (CO_3^{2-}). The absorption peaks in the range of 1000–500 cm^{-1} correspond to the stretching vibrations of metal–oxygen bonds (M-O, M=Ni/Co/Mn), which are characteristic peaks of LDH materials. The FTIR spectrum of NiCoMn-LDH@ZBC exhibited characteristic absorption peaks of both biochar (ZBC) and LDH, indicating the successful loading of LDH onto ZBC and the successful preparation of the composite material. Compared to the pre-adsorption sample, the carbonate peak intensity near 1380 cm^{-1} in the As(V)-adsorbed NiCoMn-LDH@ZBC-As(V) significantly weakened, indicating that the interlayer carbonate was replaced by As(V). A new characteristic absorption peak appeared at 756 cm^{-1}, corresponding to the stretching vibration of the As-O bond, which confirms the successful adsorption of arsenate on the material's surface or interlayers. The disappearance of the metal–oxygen (M-O, M=Ni/Co/Mn) stretching vibration peak at 649 cm^{-1} suggests an increased proportion of As-O bonds following As(V) adsorption. The hydroxyl (-OH) related peaks exhibited minor intensity changes, demonstrating coordination between surface hydroxyl groups and arsenate during the adsorption process. During adsorption, As(V) likely undergoes surface complexation with hydroxyl functional groups on the biochar surface and protonated hydroxyl groups on the LDH layered metal, ultimately forming a ternary As(V)–LDH–biochar complex [44].

To elucidate the interfacial mechanism of the adsorption process, X-ray photoelectron spectroscopy (XPS) was employed to analyze the samples before and after As adsorption. As shown in Figure 9, significant chemical shifts were observed in the characteristic peaks of C1s, O1s, and metallic elements (Zn2p/Ni2p/Co2p/Mn2p) following adsorption, indicating electron transfer and chemical interactions between the adsorbate and the active sites on the material surface. The C1s spectrum in Figure 9a reveals that after adsorption, the characteristic peaks of C-C/C=C (284.8 eV), C-O (shifted from 286.6 eV to 286.4 eV), and O-C=O (shifted from 289.7 eV to 289.3 eV) on the material surface all experienced slight shifts toward lower binding energies. This suggests an increase in the electron cloud density of carbon-containing functional groups, confirming that these sites participated in the electron transfer process with the adsorbate, potentially through hydrogen bonding or π-π interactions during the adsorption process.

The O1s spectrum shown in Figure 9b can be deconvoluted into three characteristic peaks: the lattice oxygen/metal–oxygen bond (O^{2-}, shifted from 530.3 eV to 530.8 eV), surface hydroxyl/adsorbed oxygen (-OH/O_{ads}, shifted from 531.5 eV to 531.7 eV), and adsorbed water/oxygen-containing functional groups (H_2O/O-C=O, shifted from 533.0 eV to 533.15 eV). It is observed that all O1s characteristic peaks shift toward higher binding energy after adsorption, with the lattice oxygen peak area significantly increasing and the surface hydroxyl peak intensity relatively decreasing. This indicates that surface hydroxyl groups serve as key adsorption sites and undergo surface complexation reactions with adsorbates. Meanwhile, the metal–oxygen bonds participate in interfacial complexation, leading to a reduced electron cloud density of O atoms. During the adsorption process, As(V) tends to interact with the hydroxyl groups on the material surface, thereby forming surface complexes [45,46].

In the XPS spectra of transition metal elements, the characteristic peaks of Zn2p, Ni2p, Co2p [47], and Mn2p all exhibited significant shifts after adsorption (e.g., $Zn2p_{3/2}$ shifted from 1024.8 eV to 1021.8 eV), moving toward lower binding energy. This indicates that the metal active sites gained electrons and formed stable coordination bonds with the adsor-

bate, accompanied by reversible valence changes, confirming these sites as the primary active centers for the adsorption reaction. To further elucidate the arsenic removal mechanism, high-resolution As3d spectra of the material surface were analyzed before and after adsorption, as well as after cycling (Figure S6). After adsorption, two characteristic peaks appeared in the As3d spectrum at 45.4 eV and 48.8 eV, corresponding to As(V) and As(III) species, respectively. This indicates that the material adsorbs arsenic through a synergistic oxidation–adsorption mechanism: surface oxidative sites oxidize As(III) to As(V) while simultaneously forming surface complexes with arsenate via hydroxyl groups. The As3d peak after cyclic re-adsorption exhibited a significant shift toward higher binding energy, forming more stable As-O-M inner-sphere complexes. This confirms the irreversibility of chemical adsorption and indicates partial occupation of surface active sites during cycling, which is the primary reason for the decline in cycling performance. Combined with XPS results of C1s, O1s, and metal elements, arsenic adsorption mainly relies on the synergistic effects of surface hydroxyl coordination, redox reactions, and complex formation. In conclusion, the XPS results demonstrate that the adsorption process is not merely physical adsorption but rather a synergistic multi-mechanism chemical adsorption dominated by surface complexation reactions, coupled with electron transfer, coordination reactions, and hydrogen bonding interactions. The metal sites, hydroxyl groups, and carbon-containing functional groups on the material surface collectively participate in interfacial reactions, providing abundant binding sites for adsorbates [48–50].

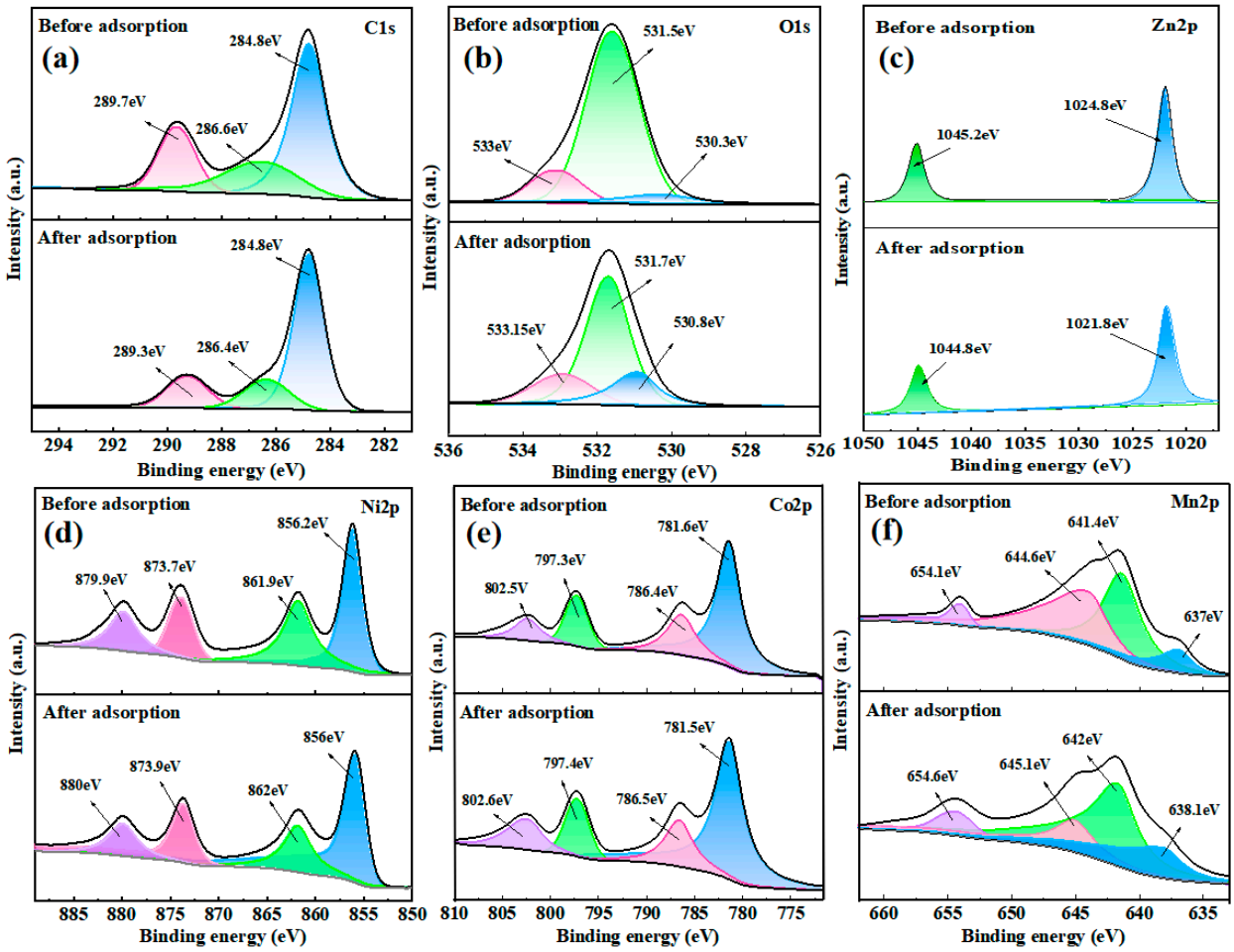


Figure 9. XPS spectra of the NiCoMn-LDHs@ZBC before and after arsenic adsorption, Among them, the arrows provide specific information about the peak positions: (**a**) C1s, (**b**) O1s, (**c**) Zn2p, (**d**) Ni2p, (**e**) Co2p, and (**f**) Mn2p spectra.

Based on the characterization analysis presented above, the mechanism of arsenic adsorption by NiCoMn-LDHs@ZBC can be summarized and a hypothesis can be proposed (Figure 10). The adsorption of arsenic from aqueous solution by NiCoMn-LDHs@ZBC involves three distinct processes. First, the surface hydroxyl groups (-OH) of NiCoMn-LDHs@ZBC participate in coordination reactions with arsenic on the surface to form complexes. As the adsorption process progresses, the metal elements (M = Ni, Co, Mn) within NiCoMn-LDHs also develop coordination bonds, ultimately leading to the formation of stable inner-sphere complexes of As-O-M. Additionally, anion exchange pathways exist in the aqueous solution, such as exchanges with CO_3^{2-}. Finally, electrostatic attraction interactions occur, representing a common pathway for adsorption. Based on the characterization results and the fitting of adsorption kinetic models, it can be concluded that the first pathway, namely coordination, is the most significant in the adsorption process.

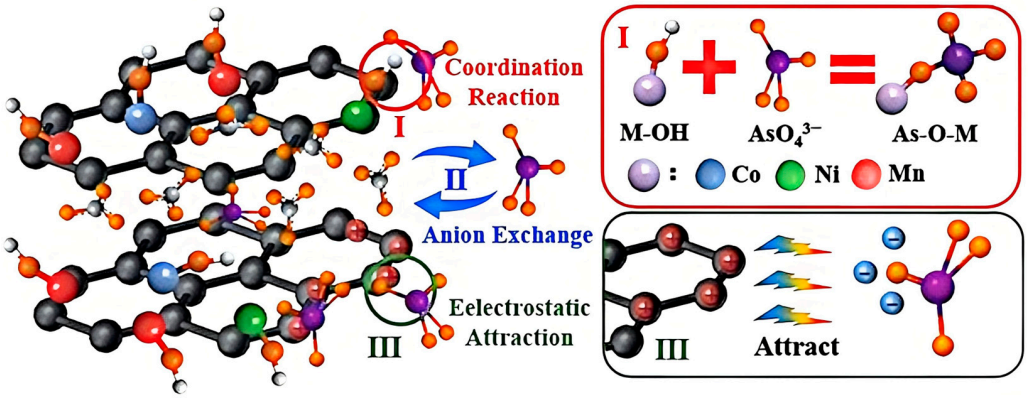


Figure 10. Schematic of As adsorption by NiCoMn-LDHs@ZBC. Gray spheres represent carbon atoms (C), orange spheres denote oxygen atoms (O), purple spheres indicate arsenic atoms (As), small white spheres symbolize hydrogen atoms (H), and other colored spheres represent various types of metal atoms (Ni/Co/Mn). The adsorption of arsenic (As) by this composite material primarily occurs through three pathways: (I) coordination; (II) ion exchange; and (III) electrostatic attraction.

3.6. Cyclic Desorption

To ensure the feasibility of the adsorbent in industrial settings, its ability to be regenerated and reused after adsorption is crucial. To investigate its reusability performance, this study conducted adsorption–desorption cycling tests. Desorption ability of As(V) loaded onto asorbents is an important when considering the suitability of a sorbent for environmental reclamation. Sodium bicarbonate ($NaHCO_3$) and sodium hydroxide (NaOH) are two commonly used agents to remove As(V) from sorbents, with desorption efficiency between 85 and 99% considered a requirement for practical use [51,52]. Due to its ability to provide high concentrations of OH^-, NaOH exhibits a significantly greater affinity for the positively charged sites on the NiCoMn layered double hydroxides (LDHs) compared to arsenate. Through anion exchange, NaOH can extensively replace both interlayer and surface-bound arsenate while simultaneously breaking the M-O-As chemical bonds, which leads to the desorption of surface-complexed arsenate and restores the adsorption activity of the material. Using a 0.1 mol/L NaOH solution as the desorption agent with a desorption time of four hours, five adsorption–regeneration cycles of NiCoMn-LDHs@ZBC for As(V) were performed.

Throughout the cycling experiments, the arsenic concentration in the solution was monitored using atomic fluorescence spectrometry. The experimental results are presented in Figure 11. After five cycles, the material still maintained an arsenic(V) removal capacity of over 55%. The specific values for adsorption capacity and arsenic removal rate for each adsorption process are presented in Table 5. The cycling results indicate that NiCoMn-

LDHs@ZBC can partially recover and sustain its high-efficiency As adsorption ability during repeated use, demonstrating strong cyclic stability.

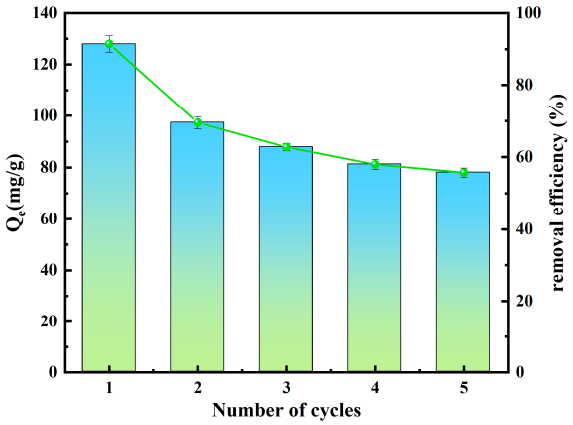


Figure 11. Recycling properties of the NiCoMn-LDHs@ZBC. Each bar chart employs a gradient color scheme to illustrate the variations in equilibrium adsorption capacity and arsenic removal rate throughout each cycle.

Table 5. Data related to the adsorption cycle process of NiCoMn-LDHs@ZBC.

Parameters	1	2	3	4	5
Q_e (mg·g^{-1})	127.99	97.30	87.86	81.18	78.03
Removal rate of As (%)	91.42	69.50	62.75	57.99	55.47

Although the overall cyclic adsorption effect of NiCoMn-LDHs@ZBC is relatively stable, it is essential to analyze the reasons for the decline in adsorption capacity, as this analysis will provide insights for the future development of more stable adsorption materials. The NiCoMn-LDHs@ZBC was characterized by X-ray diffraction (XRD) before arsenic (As) adsorption, after As adsorption, and after five cycles of As adsorption (Figure S7). The XRD patterns revealed that all three samples exhibited diffraction peaks at the (003) crystal plane, while both NiCoMn-LDHs@ZBC and NiCoMn-LDHs@ZBC-As (after one As adsorption) displayed diffraction peaks at the (006) crystal plane. However, the diffraction peak at the (006) crystal plane for the sample after five cycles of As adsorption (NiCoMn-LDHs@ZBC-As-Cycling) was particularly weak and nearly negligible. Notably, NiCoMn-LDHs@ZBC-As and NiCoMn-LDHs@ZBC-As-Cycling exhibited diffraction peaks at 24.25°, which were absent in NiCoMn-LDHs@ZBC, indicating the emergence of a new phase following arsenic adsorption. Peak searching revealed that $MnCO_3$ appeared during the adsorption process, with the peak at 24.25°corresponding to the (012) diffraction plane of $MnCO_3$. Additionally, both samples exhibited the (104) diffraction peak of $MnCO_3$ at 31.36°. Furthermore, the intensity of the (104) diffraction peak of $MnCO_3$ in the cycled sample NiCoMn-LDHs@ZBC-As-Cycling significantly increased, suggesting that the content of $MnCO_3$ gradually rose with the increase in cycling times. Thus, as the adsorption process progressed, the NiCoMn-LDHs@ZBC structure experienced a loss of metal manganese (Mn), leading to a gradual decline in the LDH structure, which was also a crucial factor contributing to the decrease in adsorption capacity. BET testing (Figure S8) was conducted on NiCoMn-LDHs@ZBC after five cycles of arsenic adsorption. The isotherm presented in Figure S8a exhibits an H3-type hysteresis loop, indicating that the material consists of slit-shaped mesopores formed by particle accumulation. This observation aligns with the conclusions drawn from the SEM (Figure 2d) and BET (Figure 3a) analyses of NiCoMn-LDHs@ZBC prior to adsorption. Figure S8b displays the pore size distribution of the material, with specific data provided in Table 2. The numerical values indicate that

after five cycles of adsorption, the specific surface area of NiCoMn-LDHs@ZBC-As(V) significantly decreased from 284.2 m^2/g to 198.7 m^2/g. This reduction is primarily attributed to the adsorption and deposition of arsenic species on the material's surface and within the pores, which occupied active sites and partially blocked the pore channels. However, the average pore diameter of the material increased after adsorption, rising from 2.97 nm to 4.61 nm. This change was likely due to the preferential blocking and disappearance of smaller pores from the pore size distribution, while larger mesoporous structures were retained. These results indicate that the mesoporous structure of the material remained stable during the adsorption process, thereby ensuring unobstructed mass transfer channels. The XPS test results of the samples after multiple adsorption cycles indicated that as the number of cycles increased, a greater number of As-O-M inner-sphere complexes formed on the surface of NiCoMn-LDHs@ZBC. Despite the use of NaOH for regeneration after each cycle, the active sites on the surface of NiCoMn-LDHs@ZBC diminished with increasing cycles, ultimately resulting in a decline in adsorption capacity.

4. Conclusions

In this study, zinc-modified biochar (ZBC) was prepared from rose willow, and the NiCoMn-LDHs@ZBC composite was synthesized via a hydrothermal method. Its characteristics and adsorption capacity for As(V) from aqueous environments were comprehensively investigated and analyzed. Experimental results demonstrated that optimal adsorption performance was achieved at pH = 5.0, with an actual adsorption capacity of 159.780 mg/g for As(V) in water treatment, significantly higher than the adsorption capacities of many previously reported adsorbents. By fitting the adsorption behavior, it was determined that the adsorption process conforms to the Langmuir isotherm model (R^2 = 0.996), indicating primarily uniform monolayer adsorption. Adsorption kinetics studies indicate that the adsorption process follows a pseudo-second-order kinetic model (R^2 = 0.998), confirming the existence of a chemisorption mechanism between As(V) and the active sites on the material surface. Based on the characterization results of the composite before and after adsorption, it is progressively verified that the entire adsorption process mainly involves three pathways: first, electrostatic attraction between the material surface and arsenic-containing ions; second, ion exchange between arsenic-containing ions and interlayer carbonate ions; and third, coordination reactions between surface hydroxyl groups (-OH) of NiCoMn-LDHs@ZBC and As, forming As-O-M inner-sphere complexes as adsorption proceeds. Additionally, the NiCoMn-LDHs@ZBC composite exhibits relatively stable reusability. Therefore, this composite possesses characteristics such as low production cost, environmental friendliness, excellent adsorption efficiency, and ease of recovery, demonstrating its potential for application in addressing arsenic pollution in wastewater treatment.

Supplementary Materials: The following supporting information can be downloaded at https://www.mdpi.com/article/10.3390/cryst16050352/s1. Figure S1: TEM image of the NiCoMn-LDH@ZBC; Figure S2: (a) N_2 adsorption-desorption isotherm and (b) pore size distribution curve of ZnBC; Figure S3: (a) N_2 adsorption-desorption isotherm and (b) pore size distribution curve of NiCoMn-LDHs; Figure S4: (a) Optimization of the molar ratio of Ni, Co, and Mn elements in NiCoMn-LDHs@ZBC. (b) Optimization of synthesis temperature for NiCoMn-LDHs in NiCoMn-LDHs@ZBC. (c) Optimization of adsorption time for As by NiCoMn-LDHs@ZBC; Figure S5: SEM images of NiCoMn-LDHs@ZBC after As adsorption; Figure S6: (a) XPS spectra of As 3d after adsorption by NiCoMn-LDHs@ZBC: (a) after first adsorption; (b) after five cycles of adsorption; Figure S7. (a) XRD spectra of As 3d after adsorption by NiCoMn-LDHs@ZBC: (a) after first adsorption; (b) after five cycles of adsorption; Figure S8: (a) N_2 adsorption–desorption isotherms and (b) pore size distribution curves of NiCoMn-LDHs@ZBC after five cycles of arsenic adsorption.

Author Contributions: Conceptualization, X.Z. and H.S.; Methodology, X.G. and X.Z.; Software, X.G. and H.Y.; Formal analysis, X.G. and H.Y.; Investigation, X.G.; Resources, X.Z.; Data curation, H.Y.; Writing—original draft, X.G.; Writing—review & editing, X.Z. and H.S.; Visualization, X.Z. and H.S.; Supervision, H.S.; Project administration, H.S.; Funding acquisition, H.S. All authors have read and agreed to the published version of the manuscript.

Funding: This study was jointly funded by the Key Research and Development and Achievement Transformation Plan of the Inner Mongolia Autonomous Region (2024KJHZ0018) and the Natural Science Foundation of the Inner Mongolia Autonomous Region (2024LHMS04017). Additionally, the Article Processing Charge (APC) was funded by the Key research and development and achievement transformation plan of Inner Mongolia Autonomous Region.

Data Availability Statement: The original contributions presented in this study are included in the article/Supplementary Material. Further inquiries can be directed to the corresponding authors.

Acknowledgments: This work was financially supported by Key research and development and achievement transformation plan of Inner Mongolia Autonomous Region (2024KJHZ0018) and Natural Science Foundation of Inner Mongolia Autonomous Region (2024LHMS04017).

Conflicts of Interest: The authors declare that they have no known competing financial interests or personal relationships that could have appeared to influence the work reported in this paper.

References

1. Smedley, P.L.; Kinniburgh, D.G. A review of the source, behaviour and distribution of arsenic in natural waters. *Appl. Geochem.* **2002**, *17*, 517–568. [CrossRef]
2. Sadiq, M.; Zaidi, T.H.; Mian, A.A. Environmental behavior of arsenic in soils: Theoretical. *Water Air Soil Pollut.* **1983**, *20*, 369–377. [CrossRef]
3. Podgorski, J.; Berg, M. Global threat of arsenic in groundwater. *Science* **2020**, *368*, 845–850. [CrossRef]
4. WHO. *Guidelines for Drinking-Water Quality*, 4th ed.; Incorporating 1st Addendum; World Health Organization: Geneva, Switzerland, 2022.
5. Dambies, L. Existing and prospective sorption technologies for the removal of arsenic in water. *Sep. Sci. Technol.* **2005**, *39*, 603–627. [CrossRef]
6. Patra, B.R.; Mukherjee, A.; Nanda, S.; Dalai, A.K. Biochar production, activation and adsorptive applications: A review. *Environ. Chem. Lett.* **2021**, *19*, 2237–2259. [CrossRef]
7. Rambabu, N.; Rao, B.; Surisetty, V.; Das, U.; Dalai, A. Production, characterization, and evaluation of activated carbons from de-oiled canola meal for environmental applications. *Ind. Crop. Prod.* **2015**, *65*, 572–581. [CrossRef]
8. Ozdemir, I.; Şahin, M.; Orhan, R.; Erdem, M. Preparation and characterization of activated carbon from grape stalk by zinc chloride activation. *Fuel Process. Technol.* **2014**, *125*, 200–206. [CrossRef]
9. Yorgun, S.; Vural, N.; Demiral, H. Preparation of high-surface area activated carbons from Paulownia wood by $ZnCl_2$ activation. *Micropor. Mesopor. Mater.* **2009**, *122*, 189–194. [CrossRef]
10. Kumar, A.; Jena, H.M. High surface area microporous activated carbons prepared from Fox nut (*Euryale ferox*) shell by zinc chloride activation. *Appl. Surf. Sci.* **2015**, *356*, 753–761. [CrossRef]
11. Shen, L.; Jiang, X.; Chen, Z.; Fu, D.; Li, Q.; Ouyang, T.; Wang, Y. Chemical reactive features of novel amino acids intercalated layered double hydroxides in As(III) and As(V) adsorption. *Chemosphere* **2017**, *176*, 57–66. [CrossRef] [PubMed]
12. Kang, D.; Yu, X.; Tong, S.; Ge, M.; Zuo, J.; Cao, C.; Song, W. Performance and mechanism of Mg/Fe layered double hydroxides for fluoride and arsenate removal from aqueous solution. *Chem. Eng. J.* **2013**, *228*, 731–740. [CrossRef]
13. Nakahira, A.; Kubo, T.; Murase, H. Synthesis of LDH-type clay substituted with Fe and Ni ion for arsenic removal and its application to magnetic separation. *IEEE Trans. Magn.* **2007**, *43*, 2442–2444. [CrossRef]
14. Li, S.; Guo, Y.; Xiao, M.; Zhang, T.; Yao, S.; Zang, S.; Fan, H.; Shen, Y.; Zhang, Z.; Li, W. Enhanced arsenate removal from aqueous solution by Mn-doped MgAl-layered double hydroxides. *Environ. Sci. Pollut. Res.* **2019**, *26*, 12014–12024. [CrossRef] [PubMed]
15. Cruz, G.; Mondal, D.; Rimaycuna, J.; Soukup, K.; Gómez, M.; Solis, J.; Lang, J. Agrowaste derived biochars impregnated with ZnO for removal of arsenic and lead in water. *J. Environ. Chem. Eng.* **2020**, *8*, 103800. [CrossRef]
16. Vamvuka, D.; Sdoukou, E.; Stratakis, A.; Pentari, D. Enhanced Adsorption of Arsenate from Contaminated Waters by Magnesium-, Zinc- or Calcium-Modified Biochar—Modeling and Mechanisms. *C* **2024**, *10*, 61. [CrossRef]
17. dos Santos Lins, P.V.; Henrique, D.C.; Ide, A.H.; de Paiva e Silva Zanta, C.L.; Meili, L. Evaluation of caffeine adsorption by MgAl-LDH/biochar composite. *Environ. Sci. Pollut. Res.* **2019**, *26*, 31804–31811. [CrossRef] [PubMed]

18. Wang, S.; Gao, B.; Li, Y.; Zimmerman, A.R.; Cao, X. Sorption of arsenic onto Ni/Fe layered double hydroxide (LDH)-biochar composites. *RSC Adv.* **2016**, *6*, 17792–17799.
19. Shiriazar, M.A.; Sepehr, E.; Maleki, R.; Khodaverdiloo, H.; Asadzadeh, F.; Dovlati, B.; Rengel, Z. Arsenate removal from aqueous solutions by Mg/Fe-LDH-modified biochar derived from apple tree residues. *Earth Environ. Sci. Trans. R. Soc. Edinb.* **2022**, *113*, 1–10. [CrossRef]
20. Hasan, I.M.U.; Bo, L.; Zhengrong, N.; Dandan, G.; Yaoling, Z.; Shakoor, M.B.; Nawaz, M.Z.; Liu, Y.; Qiao, J.; Niazi, N.K.; et al. Nano zero-valent zinc modified biochars: An innovative approach for arsenic (III) removal from synthetic and salt lake water. *J. Mol. Liq.* **2025**, *435*, 128058. [CrossRef]
21. Wang, M.; Yan, J.; Diao, Y.; Zhou, X.; Luo, T.; Wang, H.; Quan, G.; Sun, X.; Wang, J. Ball milled Mg/Al hydroxides modified nitrogen-rich biochar for arsenic removal: Performance and governing mechanism. *Carbon Res.* **2023**, *2*, 1–14. [CrossRef]
22. Gao, X.; Peng, Y.; Guo, L.; Wang, Q.; Guan, C.-Y.; Yang, F.; Chen, Q. Arsenic adsorption on layered double hydroxides biochars and their amended red and calcareous soils. *J. Environ. Manag.* **2020**, *271*, 111045. [CrossRef] [PubMed]
23. Guo, J.; Yan, C.; Luo, Z.; Fang, H.; Hu, S.; Cao, Y. Synthesis of a novel ternary HA/Fe-Mn oxides-loaded biochar composite and its application in cadmium(II) and arsenic(V) adsorption. *J. Environ. Sci.* **2019**, *85*, 168–176. [CrossRef]
24. Maziarz, P.; Matusik, J.; Strączek, T.; Kapusta, C.; Woch, W.M.; Tokarz, W.; Radziszewska, A.; Leiviskä, T. Highly effective magnet-responsive LDH-Fe oxide composite adsorbents for As(V) removal. *Chem. Eng. J.* **2019**, *362*, 207–216. [CrossRef]
25. Shao, P.; Yin, H.; Li, Y.; Cai, Y.; Yan, C.; Yuan, Y.; Dang, Z. Remediation of Cu and As contaminated water and soil utilizing biochar supported layered double hydroxide: Mechanisms and soil environment altering. *J. Environ. Sci.* **2022**, *126*, 275–286. [CrossRef]
26. Shi, H.P.; Geng, X.C.; Zhang, J.R. Experimental study on kinetics of adsorption of rare earth ions by humic acid with different molecular weight. *J. Inn. Mong. Agric. Univ. (Nat. Sci. Ed.)* **2025**, *46*, 74–81.
27. Munagapati, V.S.; Wen, H.-Y.; Wen, J.-C.; Gutha, Y.; Tian, Z.; Reddy, G.M.; Garcia, J.R. Anionic congo red dye removal from aqueous medium using Turkey tail (Trametes versicolor) fungal biomass: Adsorption kinetics, isotherms, thermodynamics, reusability, and characterization. *J. Dispers. Sci. Technol.* **2020**, *42*, 1785–1798. [CrossRef]
28. Drits, V.A.; Sokolova, T.N.; Sokolova, G.V.; Cherkashin, V.I. New Members of the Hydrotalcite-Manasseite Group. *Clays Clay Miner.* **1987**, *35*, 401–417. [CrossRef]
29. Sing, K.S. Reporting physisorption data for gas/solid systems with special reference to the determination of surface area and porosity. *Pure Appl. Chem.* **1985**, *57*, 603–619. [CrossRef]
30. Seftel, E.; Niarchos, M.; Vordos, N.; Nolan, J.; Mertens, M.; Mitropoulos, A.; Vansant, E.; Cool, P. LDH and TiO_2/LDH-type nanocomposite systems: A systematic study on structural characteristics. *Microporous Mesoporous Mater.* **2015**, *203*, 208–215. [CrossRef]
31. Xu, F.; Chen, H.; Dai, Y.; Wu, S.; Tang, X. Arsenic adsorption and removal by a new starch stabilized ferromanganese binary oxide in water. *J. Environ. Manag.* **2019**, *245*, 160–167. [CrossRef]
32. Zhang, G.; Luo, J.; Wang, L.; Zhang, X. Polyvinyl alcohol-stabilized granular Fe–Mn binary oxide as an effective adsorbent for simultaneous removal of arsenate and arsenite. *Environ. Technol.* **2019**, *41*, 2564–2574. [CrossRef]
33. Otgonjargal, E.; Kim, Y.S.; Park, S.M.; Baek, K.; Yang, J.S. Mn-Fe layered double hydroxides for adsorption of As(III) and As(V). *Sep. Sci. Technol.* **2012**, *47*, 2192–2198. [CrossRef]
34. Zou, Y.; Wang, X.; Chen, Z.; Yao, W.; Ai, Y.; Liu, Y.; Hayat, T.; Alsaedi, A.; Alharbi, N.S.; Wang, X. Superior coagulation of graphene oxides on nanoscale layered double hydroxides and layered double oxides. *Environ. Pollut.* **2016**, *219*, 107–117. [CrossRef]
35. Meng, X.; Korfiatis, G.P.; Bang, S.; Bang, K.W. Combined effects of anions on arsenic removal by iron hydroxides. *Toxicol. Lett.* **2002**, *133*, 103–111. [CrossRef]
36. Deng, Y.; Li, Y.; Li, X.; Sun, Y.; Ma, J.; Lei, M.; Weng, L. Influence of calcium and phosphate on pH dependency of arsenite and arsenate adsorption to goethite. *Chemosphere* **2018**, *199*, 617–624. [CrossRef] [PubMed]
37. Meng, X. Effects of silicate, sulfate, and carbonate on arsenic removal by ferric chloride. *Water Res.* **2000**, *34*, 1255–1261. [CrossRef]
38. Langmuir, I. The adsorption of gases on plane surfaces of glass, mica and platinum. *J. Am. Chem. Soc.* **1918**, *40*, 1361–1403. [CrossRef]
39. Freundlich, H. Über die adsorption in lösungen. *Z. Für Phys. Chem.* **1907**, *57*, 385–470. [CrossRef]
40. Tao, Q.; Chen, Y.; Zhao, J.; Li, B.; Li, Y.; Tao, S.; Li, M.; Li, Q.; Xu, Q.; Li, Y.; et al. Enhanced Cd removal from aqueous solution by biologically modified biochar derived from digestion residue of corn straw silage. *Sci. Total. Environ.* **2019**, *674*, 213–222. [CrossRef]
41. Srivastav, A.L.; Pham, T.D.; Izah, S.C.; Singh, N.; Singh, P.K. Biochar Adsorbents for Arsenic Removal from Water Environment: A Review. *Bull. Environ. Contam. Toxicol.* **2021**, *108*, 616–628. [CrossRef]
42. Boyd, G.E.; Schubert, J.; Adamson, A.W. The Exchange Adsorption of Ions from Aqueous Solutions by Organic Zeolites. I. Ion-exchange Equilibria1. *J. Am. Chem. Soc.* **1947**, *69*, 2818–2829. [CrossRef]
43. Hu, Q.; Liu, Y.; Gu, X.; Zhao, Y. Adsorption behavior and mechanism of different arsenic species on mesoporous $MnFe_2O_4$ magnetic nanoparticles. *Chemosphere* **2017**, *181*, 328–336. [CrossRef]

44. Kushwaha, R.; Singh, R.S.; Mohan, D. Comparative study for sorption of arsenic on peanut shell biochar and modified peanut shell biochar. *Bioresour. Technol.* **2023**, *375*, 128831. [CrossRef]
45. Yu, L.; Zhou, H.; Sun, J.; Qin, F.; Yu, F.; Bao, J.; Yu, Y.; Chen, S.; Ren, Z. Cu nanowires shelled with NiFe layered double hydroxide nanosheets as bifunctional electrocatalysts for overall water splitting. *Energy Environ. Sci.* **2017**, *10*, 1820–1827. [CrossRef]
46. Gong, Y.; Xu, Z.; Pan, H.; Lin, Y.; Yang, Z.; Du, X. Hierarchical Ni_3S_2 nanosheets coated on Co_3O_4 nanoneedle arrays on 3D nickel foam as an efficient electrocatalyst for the oxygen evolution reaction. *J. Mater. Chem. A* **2018**, *6*, 5098–5106. [CrossRef]
47. Xia, X.; Wang, S.; Liu, D.; Wang, F.; Zhang, X.; Zhang, H.; Yu, X.; Pang, Z.; Li, G.; Chen, C.; et al. Electronic Modulation in Cu Doped NiCo LDH/NiCo Heterostructure for Highly Efficient Overall Water Splitting. *Small* **2024**, *20*, e2311182. [CrossRef]
48. Maliyekkal, S.M.; Philip, L.; Pradeep, T. As(III) removal from drinking water using manganese oxide-coated-alumina: Performance evaluation and mechanistic details of surface binding. *Chem. Eng. J.* **2009**, *153*, 101–107. [CrossRef]
49. Sigdel, A.; Park, J.; Kwak, H.; Park, P.-K. Arsenic removal from aqueous solutions by adsorption onto hydrous iron oxide-impregnated alginate beads. *J. Ind. Eng. Chem.* **2016**, *35*, 277–286. [CrossRef]
50. Tuutijärvi, T.; Lu, J.; Sillanpää, M.; Chen, G. Adsorption Mechanism of Arsenate on Crystal γ-Fe_2O_3 Nanoparticles. *J. Environ. Eng.* **2010**, *136*, 897–905. [CrossRef]
51. Hu, X.; Ding, Z.; Zimmerman, A.R.; Wang, S.; Gao, B. Batch and column sorption of arsenic onto iron-impregnated biochar synthesized through hydrolysis. *Water Res.* **2015**, *68*, 206–216. [CrossRef] [PubMed]
52. Kumar, S.; Nair, R.R.; Pillai, P.B.; Gupta, S.N.; Iyengar, M.A.R.; Sood, A.K. Graphene Oxide–$MnFe_2O_4$ Magnetic Nanohybrids for Efficient Removal of Lead and Arsenic from Water. *ACS Appl. Mater. Interfaces* **2014**, *6*, 17426–17436. [CrossRef]

Disclaimer/Publisher's Note: The statements, opinions and data contained in all publications are solely those of the individual author(s) and contributor(s) and not of MDPI and/or the editor(s). MDPI and/or the editor(s) disclaim responsibility for any injury to people or property resulting from any ideas, methods, instructions or products referred to in the content.